

¹ Studies of uniformity of 50 μm low-gain avalanche detectors
² at the Fermilab test beam.

³ A. Apresyan^{*a}, S. Xie^b, C. Pena^b, R. Arcidiacono^{e,g}, N. Cartiglia^e, M. Carulla^h,
⁴ G. Derylo^a, M. Ferrero^e, D. Flores^h, P. Freeman^d, Z. Galloway^d, A. Ghassemiⁱ, H. Al
⁵ Ghoul^c, L. Gray^a, S. Hidalgo^h, S. Kamadaⁱ, S. Los^a, M. Mandurrino^e, A. Merlos^h,
⁶ N. Minafra^c, G. Pellegrini^h, D. Quirion^h, C. Royon^c, H. Sadrozinski^d, A. Seiden^d,
⁷ V. Sola^e, M. Spiropulu^b, A. Staiano^e, L. Uplegger^a, K. Yamamotoⁱ, K. Yamamuraⁱ

^a*Fermi National Accelerator Laboratory, Batavia, IL, USA*

^bCalifornia Institute of Technology, Pasadena, CA, USA

^c University of Kansas, KS, USA

^dSCIPP, University of California Santa Cruz, CA, USA

^eINFN, Torino, Italy

^fUniversità di Torino, Torino, Italy

⁹Università del Piemonte Orientale, Italy

^hCentro Nacional de Microelectrónica (IMB-CNM-CSIC), Barcelona, Spain

ⁱHamamatsu Photonics (HPK), Hamamatsu, Japan

17 Abstract

In this paper we report measurements of the uniformity of time resolution, signal amplitude, and charged particle detection efficiency across the sensor surface of low-gain avalanche detectors (LGAD). Comparisons of the performance of sensors with different doping concentrations and different active thicknesses are presented, as well as their temperature dependance and radiation tolerance up to 6×10^{14} n/cm². Results were obtained at the Fermilab test beam facility using 120 GeV proton beams, and a high precision pixel tracking detector. LGAD sensors manufactured by the Centro Nacional de Microelectrónica (CNM) and Hamamatsu Photonics (HPK) were studied. The uniformity of the sensor response in pulse height before irradiation was found to have a 2% spread. The efficiency and timing resolution before irradiation were found to be 100% and 30-40 ps, respectively. A “no-response” area between pads was measured to be about 70 μm for CNM and 110 μm for HPK sensors. After a neutron fluence of 6×10^{14} n/cm² the CNM sensor exhibits a large gain variation of a factor of 2.5 when comparing metallized and non-metallized sensor areas. An irradiated CNM sensor achieved a time resolution of 30 ps for the metallized area and 40 ps for the non-metallized area, while a HPK sensor irradiated to the same fluence achieved a 30 ps time resolution.

18 *Key words:*

19 Silicon, Timing, LGAD

*Corresponding author

Email address: apresyan@fnal.gov (A. Apresyan)

20	Contents		
21	1	Introduction	2
22	2	Experimental Setup	3
23	3	LGAD Sensor Properties	5
24	4	Readout Electronics	6
25	5	Timestamp Reconstruction	7
26	6	Sensor Studies and Analysis	9
27	6.1	Study of the uniformity of the LGAD sensors	9
28	6.2	Measurement of the “no-response” area between two neighboring pixels . .	11
29	6.3	Comparison of HPK doping profiles	12
30	6.4	Comparison of uniformity of HPK 50 μm with 80 μm	14
31	6.5	Temperature dependence of the LGAD sensors	17
32	6.6	Radiation tolerance of the LGADs	20
33	7	Conclusion	22

34 1. Introduction

35 Future colliders, including the high luminosity upgrade of the Large Hadron Collider
36 (HL-LHC) at CERN, will operate with an order of magnitude higher instantaneous lu-
37 minosity compared to what has been achieved at the large hadron collider (LHC) so
38 far. With the increased instantaneous luminosity, the rate of simultaneous interactions
39 per bunch crossing (pileup) is projected to reach an average of 140 to 200. The large
40 amount of pileup increases the difficulties in separating particles from the hard scatter-
41 ing interaction with those produced in different pileup interactions. In particular, the
42 ability to discriminate between jets produced in the events of interests, especially those
43 associated with vector boson fusion processes, and jets produced by pileup interactions
44 will be degraded. Additionally, the efficiency to identify high p_{T} isolated electrons and
45 muons will be severely reduced due to the high density of pileup particles in their vicinity.
46 The missing transverse energy resolution will also deteriorate, and several other physics
47 objects performance metrics will also suffer the detrimental effects of pileup.

48 One way to mitigate the pileup effects mentioned above, complementary to precision
49 tracking methods, is to perform a time of arrival measurement associated with each par-
50 ticle. Such a measurement with a precision of about 30-40 ps, will reduce the effective
51 amount of pileup by a factor of 10, given that the spread in collision time of the pileup
52 interactions at HL-LHC is foreseen to be approximately 200 ps. It has been previously
53 shown that a precision of better than 20 ps can be achieved for electromagnetic showers
54 measured with silicon sampling calorimeters [1–3] using traditional planar silicon detec-
55 tors. In this paper, we report results of particle beam measurements with thin low-gain
56 avalanche detectors (LGAD) that have been shown to achieve time resolutions around
57 30 ps [4, 5]. LGAD are envisioned to be used in the CMS and ATLAS experiment
58 upgrades for HL-LHC in order to reduce the pileup contamination. The implemented

regions of pseudorapidity (η) are: $|\eta| > 1.5$, and $2.4 < |\eta| < 4.2$ for CMS and ATLAS, respectively. In order to achieve the desired timing precision across a large area of the detectors, the sensors will need to provide high uniformity of signal response and timing resolution. In this paper, we perform detailed measurements of the performance of LGAD sensors produced by Centro Nacional de Microelectrónica (CNM) and Hamamatsu Photonics (HPK) exposed to the 120 GeV proton beam at Fermilab. Utilizing high-precision tracking detectors we extract position dependence of the charged-particle detection efficiency, signal pulse height, signal timestamp, and time resolution. We also compare the uniformity of 50 and 80 μm LGAD sensors, as well as the HPK and CNM sensors irradiated to an equivalent neutron flux of $6 \times 10^{14} \text{ n/cm}^2$. Detailed measurements of irradiated HPK sensors were presented in Ref. [6].

The paper is organized as follows: the experimental setup is described in Sec. 2; the tested LGAD sensors and their operating conditions are listed in Sec. 3; readout electronics used in the measurements are described in Sec. 4; algorithms used in the event reconstruction are described in Sec. 5; beam test results are presented in Sec. 6, followed by the conclusion in Sec. 7.

2. Experimental Setup

Test-beam measurements were performed at the Fermilab Test-beam Facility (FTBF) which provided a 120 GeV proton beam from the Fermilab Main Injector accelerator. The Devices Under Test (DUTs) were mounted on a remotely operated motorized stage, placed inside the pixel telescope detector [7]. The latter provides better than 10 μm position resolution for charged particles impinging on the DUT. Additionally, a Photek 240 micro-channel plate (MCP-PMT) detector [8–11] was placed furthest downstream, and provided a very precise reference timestamp. Its precision has been previously measured to be less than 7 ps [10]. A schematic diagram and photograph of the experimental area are shown in Fig. 1 and Fig. 2, respectively.

The DAQ system for the DUTs and the Photek MCP-PMT is based on a CAEN V1742 digitizer board [12], which provides digitized waveforms sampled at 5 GS/s, and with one ADC count corresponding to 0.25 mV. The CAEN digitizer was voltage- and time-calibrated using the procedure described in Ref. [13]. The electronic time resolution of the CAEN V1742 digitizer was measured to be less than 4 ps, and thus, its impact on the timing measurements presented in these studies can be neglected. The DAQ for the pixel telescope is based on the CAPTAN system developed at Fermilab [7]. The track reconstruction is performed using the Monicelli software package developed specifically for the test-beam application.

The DUTs were placed inside the telescope box described in Ref.[7], and mounted on an aluminum mechanical support structure. The telescope box can be moved remotely in both the horizontal and vertical directions in order to align the DUTs with the beam. The aluminum support structure for the DUTs provide both mechanical stability and are equipped with Peltier cooling elements that were used in this study to operate the DUTs at -10° and -20° C.

The beam is resonantly extracted in a slow spill for each Main Injector cycle delivering a single 4.2 sec long spill per minute. The primary beam (bunched at 53 MHz) consists of high energy protons (120 GeV) at variable intensities between 1 and 300 kHz. The trigger to both the CAEN V1742 and to the pixel telescope was provided by a scintillator

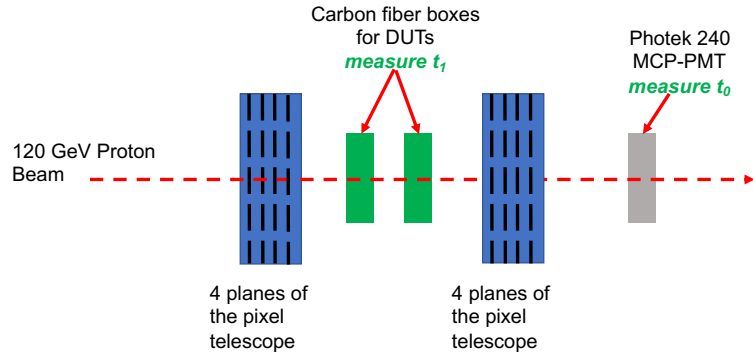


Figure 1: A schematic diagram of the test-beam setup is shown. The t_0 and t_1 are defined in Section 4.

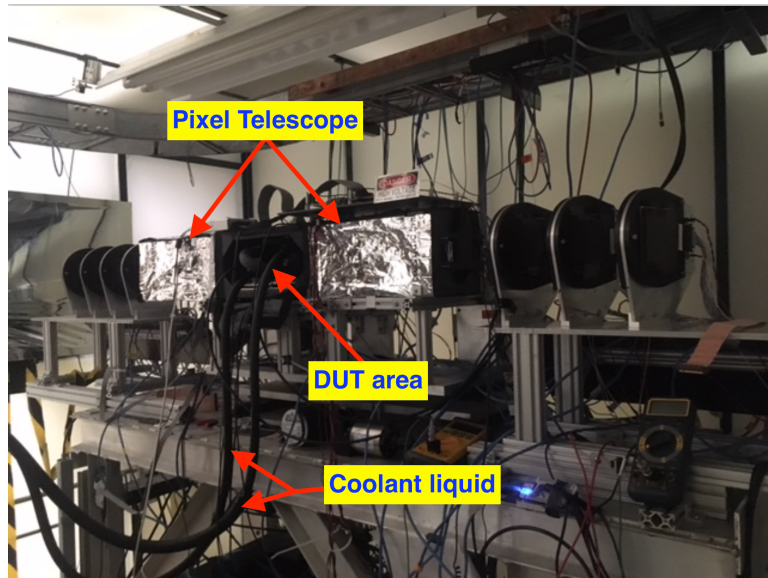


Figure 2: A picture of the experimental area. The pixel telescope detectors are placed inside the electrostatic-discharge shielded boxes on the two sides of the DUT area. Cooling liquid for the Peltier elements inside the DUT area is provided by the two tubes shown in the picture.

104 mounted on a photomultiplier tube, placed upstream of the DUTs in the beam-line. Due
 105 to the limited buffer depth of the CAEN V1742 board, special care had to be taken in
 106 the design of the DAQ system to ensure that both the DUT and telescope DAQs collect
 107 exactly the same amount of triggers. This was achieved by limiting the trigger rate by
 108 introducing an adjustable dead-time using a custom-designed trigger board. This trigger
 109 board is the combination of a custom FPGA board (the CAPTAN+x, equipped with
 110 multiple FPGA Mezzanine Card connectors and gigabit ethernet connectivity) mated
 111 to a front end board (the NIM+, with multiple inputs and outputs, each supporting
 112 a variety of interface levels such as NIM, LVDS, and TTL). The combined board is
 113 shown in Fig. 3 and was used to interface to photomultiplier signals through on-board
 114 programmable discriminators, and to form trigger signals with software configurable
 115 time-based veto and pre-scaler event filtering. We found that at a rate of about 1,500
 116 triggers per spill the CAEN V1742 and pixel telescope maintained full synchronization.
 117 Processed data from the pixel telescope and the DUTs were merged offline by matching
 118 the trigger counters recorded by the two systems.



Figure 3: The custom-made trigger board composed of NIM+ and CAPTAN+x boards.

119 3. LGAD Sensor Properties

120 Sensors manufactured by HPK and CNM were measured in the test beam experiment.
 121 Both single- and four-channel configurations of the sensor were used in the measurements.
 122 The sensors studied have active thicknesses of about $50 \mu\text{m}$ and $80 \mu\text{m}$.
 123 CNM sensors have an active thickness of about $45 \mu\text{m}$ and were produced on 4-inch
 124 Silicon-on-Insulator wafers with a $45 \mu\text{m}$ thick high resistivity float zone (FZ) active layer
 125 on top of a $1 \mu\text{m}$ buried oxide and a $300 \mu\text{m}$ support wafer. The back-side contact is
 126 achieved through wet-etched deep access holes through the insulator. Details on CNM
 127 sensors can be found in Ref. [4, 14].

128 The HPK sensors were manufactured on 6-inch silicon wafers of $150\ \mu\text{m}$ total thickness
 129 with a $50\ \mu\text{m}$ or $80\ \mu\text{m}$ thick high resistivity float zone (FZ) active layer. Four gain splits,
 130 identified with the letters A (lowest gain) to D (highest gain), were produced identical
 131 in the mask design but with a different p^+ dose of the gain layer to study the optimal
 132 parameters of the charge multiplication mechanism. The pads were produced in three
 133 versions: two with guard ring (GR and GBGR) and one without guard ring. Four-channel
 134 sensors in a 2×2 array were produced with all 4 gain-splits, and are identified with the
 135 PIX identifier. For example, the 2×2 array of the $50\ \mu\text{m}$ sensor split D is labelled
 136 as 50D-PIX. The sensor corresponding to each of the four channels in the array is also
 137 referred to as a pixel in this paper. Each pixel in the 2×2 HPK array has dimensions
 138 of $3 \times 3\ \text{mm}^2$. The CNM single-channel sensors are square pads with an active area of
 139 $1.7\ \text{mm}^2$ while the HPK single-channel sensors are circular pads with an active area of
 140 $0.8\ \text{mm}^2$.

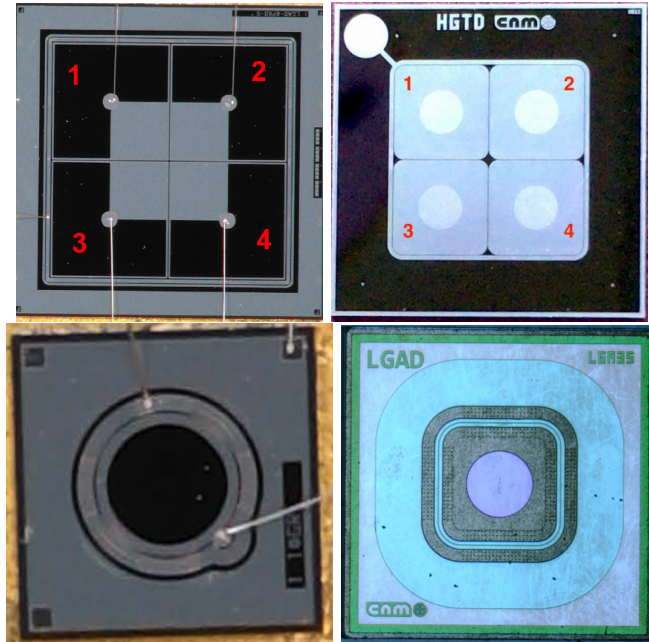


Figure 4: Photographs of the HPK 50D-PIX 2×2 array sensor (top left), the CNM-W9HG11 2×2 array sensor (top right), the 50D-GR single sensor (bottom left), and the CNM W11LGA35 single sensor (bottom right) are shown. Numerical labels overlaid on top of the images of the array sensors are used in the text when referring to individual pixels.

141 4. Readout Electronics

142 Three readout electronics boards were used in various measurements presented in this
 143 paper. They were independently developed at Fermi National Accelerator Laboratory
 144 (FNAL), at the University of Kansas (KU), and at the University of California Santa
 145 Cruz (UCSC).

Sensor	Number of channels	Single channel dimensions	Single channel capacitance
HPK 50A-PIX	4	$3 \times 3 \text{ mm}^2$	20 pF
HPK 50B-PIX	4	$3 \times 3 \text{ mm}^2$	20 pF
HPK 50C-PIX	4	$3 \times 3 \text{ mm}^2$	20 pF
HPK 50D-PIX	4	$3 \times 3 \text{ mm}^2$	20 pF
HPK 80C-PIX	4	$3 \times 3 \text{ mm}^2$	12 pF
HPK 50D	1	$\varnothing = 1.0 \text{ mm}$	2.9 pF
CNM-W9HG11	4	$3 \times 3 \text{ mm}^2$	22 pF
CNM-W11LGA35	1	$1 \times 1 \text{ mm}^2$	3.9 pF

Table 1: Linear dimensions and capacitances of the sensors used in these studies.

The 4-channel Fermilab LGAD test board is designed to test sensors up to 8.5 mm by 8.5 mm at voltages up to 1 kV. Four wire-bonding pads allow for signal readout via amplifiers based on Mini-Circuits GALI-66+. The amplifiers feature transformers with 1:2 input impedance matching, two stages of amplification and a 500 MHz low-pass filter. In this full configuration, the amplifiers feature 12.5Ω input impedance, $5 \text{ k}\Omega$ transimpedance, 500 MHz bandwidth and 1 mV rms output noise. If needed it is possible to jump the input transformer and/or the low-pass filter, which would result in an input impedance of 50Ω , transimpedance of $10 \text{ k}\Omega$, and bandwidth of 2 GHz.

The 2-channel KU board, designed and produced by the University of Kansas, can accommodate many types of sensors including diamond, silicon, LGAD or avalanche photodiodes (APD). The sensor is hosted on the board itself and the electronics was optimized for precise timing measurements. In particular, the amplifier, made with discrete components, has an input impedance of 700Ω , an output noise of 4 mV and a gain in transresistance of about $50 \text{ mV}/\mu\text{A}$ with a 3 dB bandwidth of 100 MHz. Those values were simulated for an input capacitance of 20 pF, which corresponds roughly to an LGAD of 9 mm^2 . The power consumption of the board is about 130 W per channel.

The UCSC 1-channel board is described in detail in Ref. [4]. This board uses discrete components and contains several features which allow for maintaining a wide bandwidth ($\sim 2 \text{ GHz}$) and a low noise even in noisy environments. The inverting amplifier uses a high-speed SiGe transistor which has a transimpedance of about 470Ω . A commercial inverting amplifier with gain 10x is used to boost the signal. The 4-channel UCSC board has two stages: the first one is identical to the UCSC single channel board, and is followed by an inverting stage. The total transimpedance is $10.7 \text{ k}\Omega$.

5. Timestamp Reconstruction

As discussed in Section 2, the reference time is measured using the Photek MCP-PMT detector. The timestamp for this reference detector is obtained by fitting the peak region of the pulse to a Gaussian function and the mean parameter of the Gaussian is assigned as the timestamp t_0 . A more detailed description can be found in Ref [8].

The timestamp for signals from the LGAD sensors is obtained in two different ways depending on which read-out board was used. For the KU board, which has a slower decay time, the timestamp is obtained by performing a linear fit to the rising edge of the pulse, between 15% and 70% of the maximum amplitude, and the time at which the pulse reaches 45% of the maximum amplitude is assigned as its timestamp t_1 . We refer to this algorithm as the constant fraction discriminator (CFD) method. For the

180 FNAL and UCSC boards, which have fast decay times, the timestamp is obtained via
 181 a fit to a Gaussian function analogous to what is done for the reference detector. This
 182 procedure is slightly different compared to previous studies of LGAD sensors, where the
 183 CFD method was used uniformly.

184 The above choices of timestamp reconstruction algorithms used are motivated by the
 185 result of a dedicated study of different timestamp reconstruction algorithms for each of
 186 the three readout boards. The study is performed using signals from the HPK 50D sen-
 187 sor. Constant fraction discriminant (CFD) and constant threshold discriminant (CTD)
 188 algorithms are used and the time resolution performance is studied as a function of the
 189 threshold used. In Tables 2 and 3, we show the time resolution obtained for different
 190 thresholds for the CFD and CTD algorithms respectively, for the KU readout board. For
 191 the CFD algorithm, we observed no significant dependence of the timestamp on the pulse
 192 height of the signal. However, for the CTD algorithm, the timestamp does depend on
 193 the pulse height and requires a correction referred to as a time-walk correction. For most
 194 situations, the time-walk correction can be accurately described by a linear function,
 195 however we do observe that as the CTD threshold increases, the time-walk correction
 196 becomes more quadratic. In Table 3, the time resolution is reported for both linear and
 197 quadratic time-walk corrections. We observe that the best results are obtained for a
 198 CFD threshold at 45%. However the CTD algorithm at a moderate threshold does yield
 199 comparable time resolutions.

CFD Threshold	Time Resolution
15%	45 ps
30%	40 ps
45%	38 ps
60%	39 ps

Table 2: Time resolution measured for the HPK 50D-PIX sensor on the KU readout board using the constant fraction discriminant algorithm.

CTD Threshold	Time Resolution (Linear Time-walk Correction)	Time Resolution (Quadratic Time-walk Correction)
12 mV	52 ps	51 ps
18 mV	46 ps	45 ps
24 mV	43 ps	42 ps
37 mV	41 ps	40 ps
49 mV	43 ps	39 ps
61 mV	43 ps	39 ps
73 mV	45 ps	40 ps

Table 3: Time resolution measured for the HPK 50D-PIX sensor on the KU readout board using the constant threshold discriminant algorithm.

200 In Table 4, we show the analogous study performed for the FNAL and UCSC readout
 201 boards. As signals on these readout boards have fast decay times, the Gaussian fit yields
 202 the best performance. As for the KU readout board, the CFD and CTD algorithms again
 203 give similar performance for the FNAL and UCSC readout boards.

Timestamp Algorithm Type	Time Resolution (FNAL Board with HPK 50D-PIX Sensor)	Time Resolution (UCSC Board with irradiated HPK 50D Sensor)
Gaussian Fit	42 ps	35 ps
CFD at 15% Threshold	71 ps	47 ps
CFD at 30% Threshold	60 ps	42 ps
CFD at 45% Threshold	53 ps	39 ps
CFD at 60% Threshold	56 ps	44 ps
CTD at 18 mV Threshold (Linear Time-walk Correction)	55 ps	43 ps
CTD at 18 mV Threshold (Quadratic Timewalk Correction)	52 ps	37 ps

Table 4: Time resolution measured for the HPK 50D-PIX sensor on the FNAL readout board and the irradiated HPK 50D sensor on the UCSC board for a variety of timestamp reconstruction algorithms.

204 6. Sensor Studies and Analysis

205 We present a number of different studies performed on the LGAD sensors described
 206 in Section 3. They include signal response uniformity, gap distance between adjacent
 207 pixels, doping profile and sensor thickness characterization, temperature and irradiation
 208 dependence, and timing resolution. A brief overview of the analysis methods is given
 209 below, followed by subsections describing the details and results of each study.

210 Events are required to have a signal in the Photek MCP-PMT consistent with a
 211 minimum ionizing particle (MIP), and a signal above the noise in LGAD sensors. The
 212 MIP signal selection in the Photek MCP-PMT is the same for all runs and requires that
 213 the signal amplitude is between 160 mV and 320 mV. The signal selection for LGAD
 214 boards was optimized for each board individually, by selecting the MIP signal peak fitted
 215 with a Landau function. All measurements other than those described in Sec. 6.5 and
 216 6.6 were performed at room temperature.

217 Here, and in the remainder of this article, whenever a scan of a certain characteristic
 218 quantity – e.g. time resolution – of the sensor is presented, we show the X-axis scan for
 219 pixels 1 and 2, and the Y-axis scan for pixels 1 and 3, as defined on the left picture in
 220 Fig. 4. The X-axis scan across pixels 3 and 4, and Y-axis scan across pixels 2 and 4 show
 221 qualitatively the same features, and are not presented here.

222 6.1. Study of the uniformity of the LGAD sensors

223 We present in detail uniformity studies – including signal detection efficiency, most
 224 probable value, time difference, and time resolution – across the sensitive area of the
 225 LGAD. The sensors under study were produced by HPK and CNM. The largest dataset
 226 was collected for the HPK 50D-PIX and the CNM W9HG11 sensors. The HPK 50D-PIX
 227 sensor was mounted on the 4-channel FNAL board and biased to -300 V, while the CNM
 228 W9HG11 sensor was mounted on the 4-channel UCSC board and biased to -180 V. Both
 229 sensors were operated at room temperature for these studies.

230 The measurements of the particle detection efficiency are shown in Fig. 5. Efficiency
 231 is defined as the ratio of events that register a signal above the noise level in the LGAD
 232 sensor to those that contain a track identified by the pixel telescope pointing at the LGAD
 233 sensor. We observe a flat 100% efficiency across the whole sensor area. The left edge in
 234 the X-axis scan of pixel 1 on HPK 50D-PIX sensor in Fig. 5 is outside the acceptance
 235 of the pixel telescope, hence the efficiency curve does not fully cover its surface. A clear

236 drop in efficiency is observed in the transition (“no-response”) region between the two
 237 pixels. A more detailed study of the “no-response” region is given in Sec. 6.2.

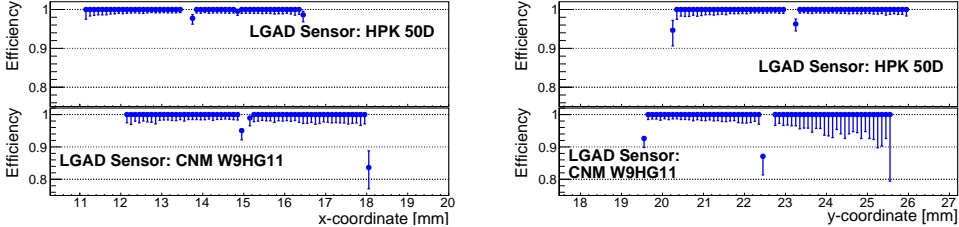


Figure 5: Efficiency measurement across the X-axis (left) and Y-axes (right) of the HPK 50D-PIX sensor mounted on the FNAL board, and the CNM W9HG11 sensor mounted on the UCSC board. The scans of pixels 1 and 2 along the X-axis, and pixels 1 and 3 along the Y-axis are shown. The pixel numbering scheme is defined in Fig. 4.

238 An important characteristic is the uniformity of the signal size across the surface of
 239 the sensor, which directly impacts its timing performance. We use the signal amplitude as
 240 the metric to characterize the signal size uniformity. The distribution of the LGAD signal
 241 amplitudes is fit to a Landau distribution. The most probable value (MPV) parameter
 242 of the fitted Landau distribution is plotted in Fig. 6. A flat response with a uniform
 243 signal size is observed over the whole sensor area.

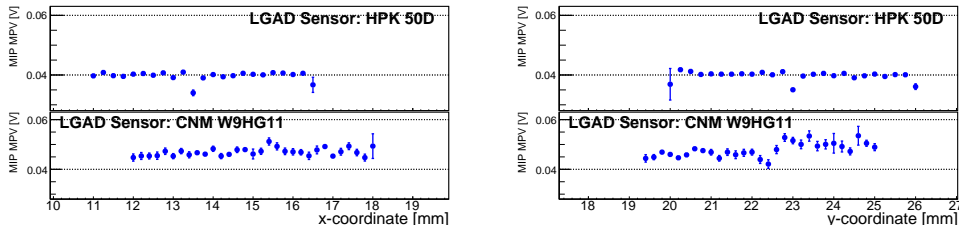


Figure 6: Signal amplitude MPV measurement across the X-axis (left) and Y-axes (right) of the HPK 50D-PIX sensor mounted on the FNAL board, and the CNM W9HG11 sensor mounted on the UCSC board. The scans of pixels 1 and 2 along the X-axis and pixels 1 and 3 along the Y-axis are shown. The pixel numbering scheme is defined in Fig. 4.

244 The measurements of the time difference $\Delta t = t_1 - t_0$ between the reference timestamp
 245 (t_0) and the timestamp of the LGAD sensors (t_1) are shown in Fig. 7. The micro-bonding
 246 scheme of the HPK and CNM 2×2 sensor arrays is shown in Fig. 4. For the HPK sensor,
 247 the Δt dependence on the hit position indicates a shift of about 20–30 ps between the
 248 metallized area near the center of the array (gray region of the top-left image in Fig. 4)
 249 and the non-metallized area. A possible explanation for this effect is a small difference in
 250 the rise time of the pulses that originate from the passage of particles in the metallized
 251 and non-metallized areas. This effect cannot be attributed to the algorithm used to time-
 252 stamp the events, since the same behavior is observed with the CFD and CDT algorithms.
 253 Furthermore, the same behavior is observed on all HPK sensor varieties mounted on KU
 254 board, as presented in Sec. 6.3. The results for the CNM sensor also show hints of this
 255 behavior, though the larger statistical uncertainties make it less significant.

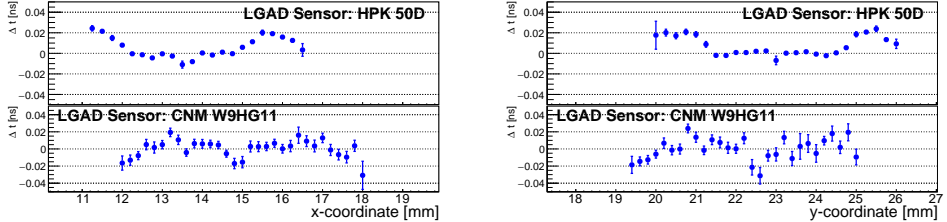


Figure 7: Δt measurement across the X- and Y-axes of the HPK 50D-PIX sensor mounted on the FNAL board. The scans of pixels 1 and 2 along the X-axis, and pixels 1 and 3 along the Y-axis are shown. The pixel numbering scheme is defined in Fig. 4.

256 The measurement of the time resolution across the sensor surface is shown in Fig. 8.
 257 The distribution of Δt between the timestamp of the LGAD signal and the reference
 258 signal is fitted with a Gaussian function, and the spread σ of the fitted function is
 259 defined as the time resolution. We observe a uniform time resolution around 40 ps across
 260 the whole surface area for HPK, and around 55 ps for CNM sensors.

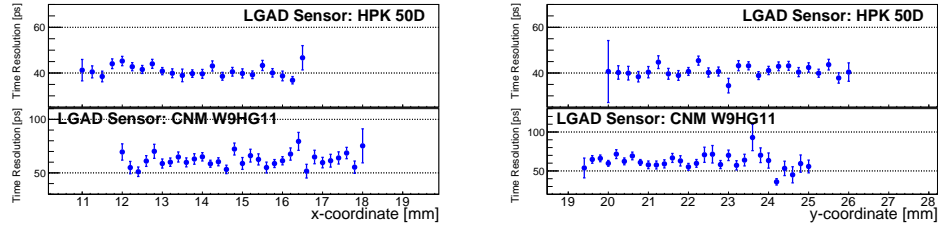


Figure 8: Time resolution measurement across the X-axis (left) and Y-axes (right) of the HPK 50D-PIX sensor mounted on the FNAL board, and the CNM W9HG11 sensor mounted on the UCSC board. The scans of pixels 1 and 2 along the X-axis, and pixels 1 and 3 along the Y-axis are shown. The pixel numbering scheme is defined in Fig. 4.

261 6.2. Measurement of the “no-response” area between two neighboring pixels

262 In order to precisely measure the width of the no-response area between two neighbor-
 263 ing pixels, a large statistics sample of about 350,000 events was collected with the
 264 HPK 50D-PIX sensor mounted on a 2-channel KU board. The sensor was biased to
 265 -300 V. The large dataset allowed us to perform a detailed scan in the area between
 266 the two pixels as shown in Fig. 9. In order to estimate the width of the no-response
 267 between the pixels, the efficiency curves of the two neighboring pixels are fitted with an
 268 S-curve function of the form $y = p_1 \times \text{erf}\{\pm(p_2 - x)/p_3\} + p_4$, where erf is the error
 269 function, and p_i are floated in the fit. We define the width of the “no-response” area as
 270 the distance between the half-maxima of the two fitted S-curves, as shown in Fig. 9. We
 271 measure the width of the no-response area on the HPK 50D-PIX sensor to be 110 μm ,
 272 with an uncertainty of 10 μm .

273 A further measurement was made on the 4-channel UCSC board for the HPK 50C-
 274 PIX sensor and the CNM W9HG11 sensor. We compare the width of the gap region of
 275 the HPK and CNM sensors in Fig. 10. Both sensors in this comparison were tested in

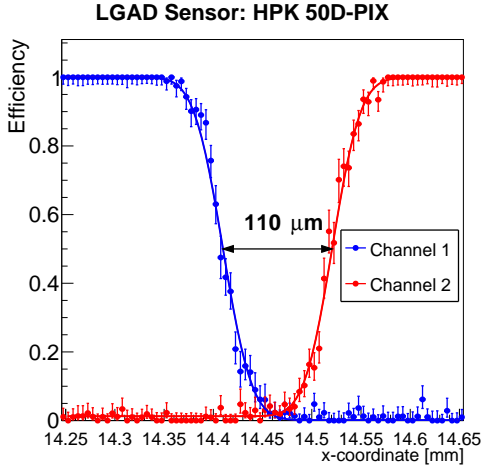


Figure 9: A zoom-in version of the efficiency measurement as a function of the X position of the beam particle. The HPK 50D-PIX sensor was operated at -300 V bias voltage. The pixel numbering scheme is defined in Fig. 4.

the beam simultaneously. The HPK 50C-PIX sensor was operated at -450 V, and CNM W9HG11 sensor was operated at -180 V. We measure the size of the “no-response” region to be around $110\text{ }\mu\text{m}$ on the HPK 50C-PIX – compatible with the HPK 50D-PIX sensor – and around $70\text{ }\mu\text{m}$ for the CNM sensor. Both measurements have an uncertainty of $10\text{ }\mu\text{m}$.

6.3. Comparison of HPK doping profiles

Studies of the dependence of the sensors’ characteristics on the doping concentrations were performed by comparing the $50\text{ }\mu\text{m}$ HPK PIX sensors of different gain splits. In order to reduce the impact of the variations between different readout boards, all measurements presented in this section were performed using only 2-channel KU readout boards. Four readout boards were prepared, each with an HPK sensor mounted on it, and tested in the beam. Data taken with the HPK 50D-PIX is the same as that presented in Fig. 9, which is the largest data sample collected during this test beam campaign. Therefore, the statistical uncertainties in the measurements of the HPK 50A-, B-, and C-PIX sensors are larger than those of 50D-PIX. For this study, the sensors were operated at room temperature, and their bias voltages were set to -630 V, -550 V, -400 V, and -300 V for the HPK 50A-PIX, HPK 50B-PIX, HPK 50C-PIX, and HPK 50D-PIX sensors, respectively.

The distribution of the MPV of signal amplitudes across the sensor area is shown in Fig. 11, where the MPV is extracted as described in Sec. 6.1. Comparing the signal amplitudes between the two pixels we observe that the average amplitude varies between the two channels. However, in Fig. 6 we observed that the amplitudes in the two pixels of the same HPK 50D-PIX sensor on the FNAL readout board do not show the same variations. We conclude that the observed difference in amplitude is due to imperfections in the manufacturing process of the custom-designed pre-amplifiers used in the KU

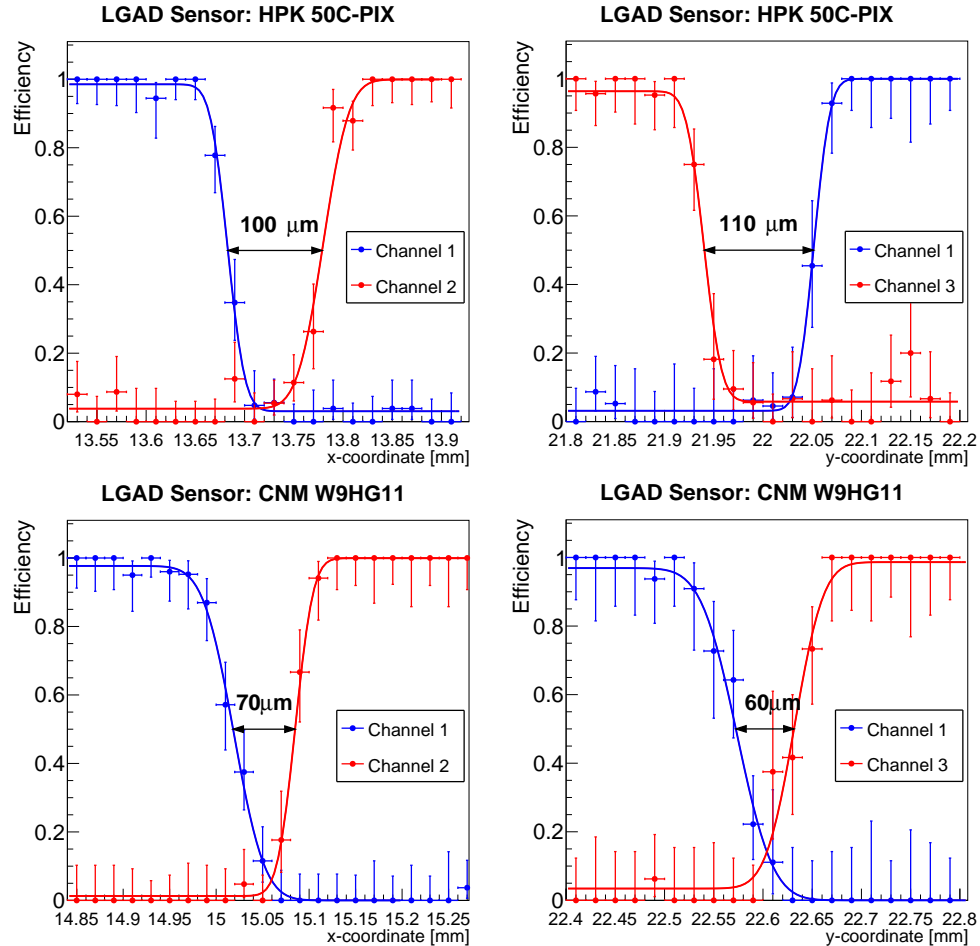


Figure 10: A zoom-in version of the efficiency measurement across the X- and Y-axes of the HPK 50C-PIX (top) and CNM W9HG11 (bottom) sensors. HPK sensor is operated at -450 V, and CNM sensor is operated at -180 V. Data points in blue are those from one pixel, and data points in red are from the neighboring pixel. The blue and red curves are fitted to the data points as described in the text. Arrows indicate the distance between the half-maximum points of the fitted curves.

301 readout board and not due to sensor properties. Nevertheless, the signal MPV within a
 302 single pixel is highly uniform for all tested samples.

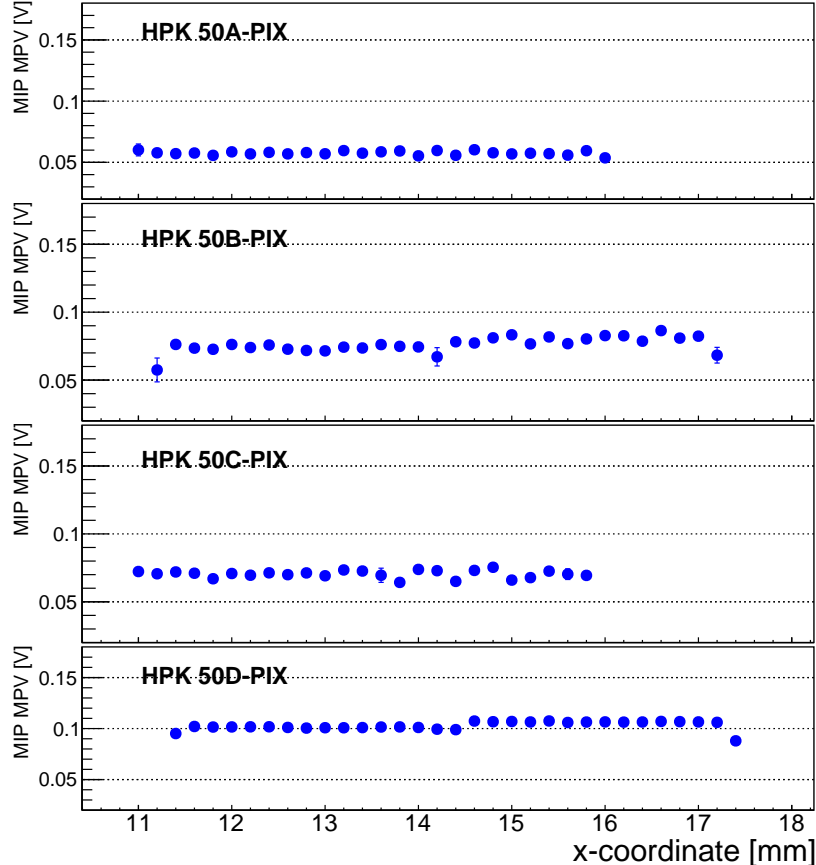


Figure 11: Signal amplitude MPV measurement across the X-axis of the HPK 50A-, 50B-, 50C-, and 50D-PIX sensors mounted on the KU board. The scan of pixels 1 and 2 along the X-axis, and pixel numbering scheme is defined in Fig. 4.

303 The measurements of the time difference between the reference timestamp and the
 304 timestamps of the HPK sensors are shown in Fig. 12. As was shown in Fig. 7, the Δt
 305 exhibits an offset of about 20 ps between the metallized area and the non-metallized area
 306 of the sensor. The feature is present in all 4 types of the HPK PIX sensors, does not
 307 depend on the readout board or timestamp reconstruction algorithm used, and appears
 308 to be statistically consistent in shape and magnitude.

309 The measurements of the time resolution across the sensors are shown in Fig. 13. We
 310 observe a uniform time resolution around 40 ps across the entire sensor area.

311 6.4. Comparison of uniformity of HPK 50 μm with 80 μm

312 The thickness of the active area of the sensor is an important design parameter when
 313 optimizing for time resolution. A detailed study of time resolution of HPK sensors of 80

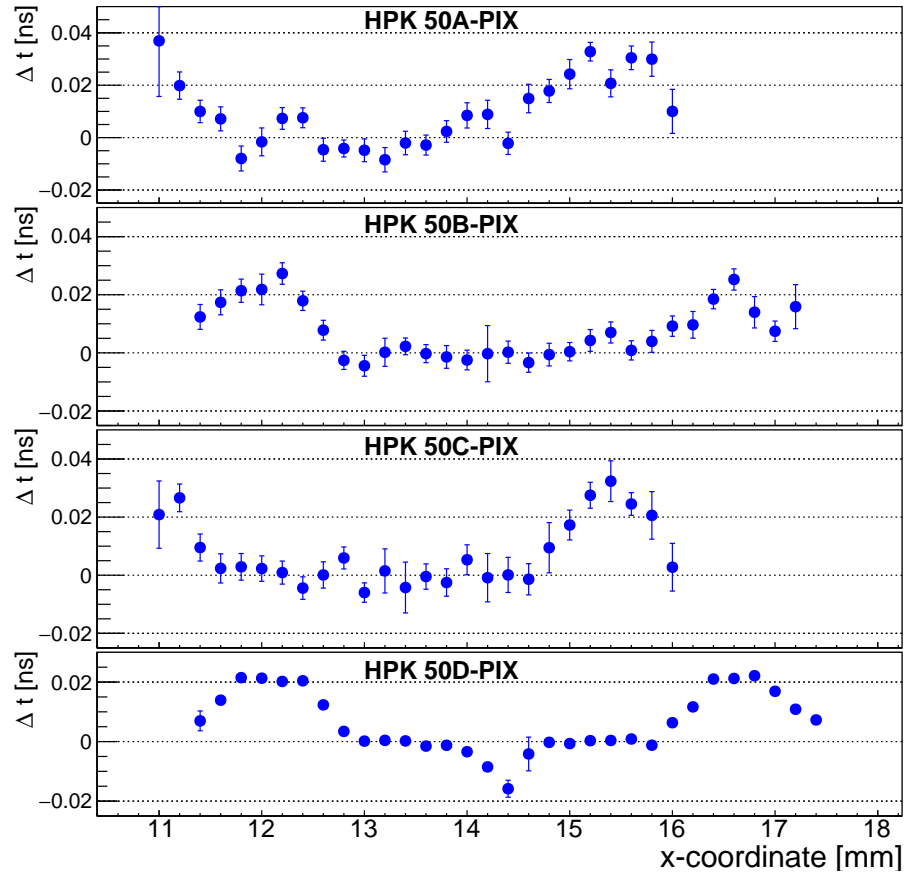


Figure 12: Δt measurements as a function of the X position of the beam particle for the HPK 50A-, 50B-, 50C-, and 50D-PIX sensors mounted on the KU board. The scan of pixels 1 and 2 along the X-axis is shown. The pixel numbering scheme is defined in Fig. 4.

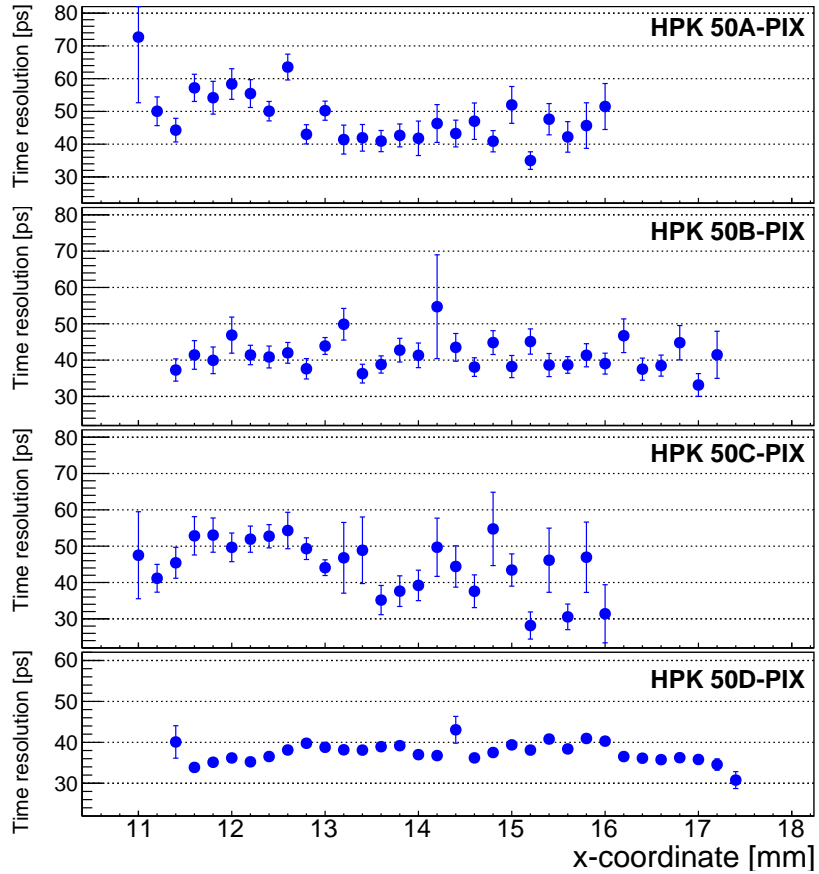


Figure 13: Time resolution measurements as a function of the X position of the beam particle for the HPK 50A-, 50B-, 50C-, and 50D-PIX sensors mounted on the KU board. The scan of pixels 1 and 2 along the X-axis is shown. The pixel numbering scheme is defined in Fig. 4.

314 and $50\ \mu\text{m}$ is presented in [6]. Here we compare the uniformity of the time resolution
 315 across the sensors of these two thicknesses. This study is performed using the HPK
 316 C-PIX sensors with the same dopant concentration. The $80\ \mu\text{m}$ sensor HPK 80C-PIX
 317 is biased at $-610\ \text{V}$, while the $50\ \mu\text{m}$ sensor HPK 50C-PIX is biased at $-400\ \text{V}$. The
 318 sensors's gains at these bias voltages are: about 11 for the $80\ \mu\text{m}$ sensor, and about 14
 319 for the $50\ \mu\text{m}$ sensor. The time resolution for the two sensors are shown in Fig. 14 as
 320 a function of position, and exhibit fairly uniform behavior. Measurements of the HPK
 321 50C-PIX sensor were performed on the KU 2-channel board, and those for HPK 80C-PIX
 322 used the FNAL 4-channel board.

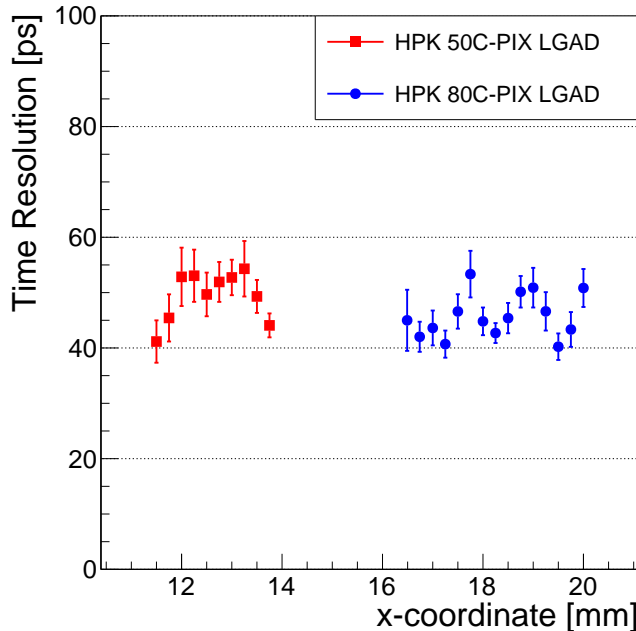


Figure 14: Comparison of the uniformity of the measured time resolution of the HPK 80C-PIX versus
 50C-PIX sensors. The $80\ \mu\text{m}$ sensor is mounted on the FNAL board, and is biased at $-610\ \text{V}$, and the
 50C-PIX sensor is mounted on the KU board and is biased at $-400\ \text{V}$.

323 6.5. Temperature dependence of the LGAD sensors

324 In order to maintain their optimal performance at the highest fluences envisioned at
 325 the HL-LHC, the LGAD sensors will be cooled to temperatures below -20°C degrees.
 326 Operation at such low temperatures will allow to significantly reduce the leakage current,
 327 and additionally improve the timing characteristics of the sensors. In this section we de-
 328 scribe the measurements of the LGAD sensors performed at -10 and -20°C degrees, and
 329 compare the results to those at room temperature. These measurements were performed
 330 with the HPK 50D-PIX sensors mounted on the FNAL 4-channel board. The sensor was
 331 biased at the same voltage of $-250\ \text{V}$ for all temperature scenarios. The HPK 50D gain

332 at this bias voltage and at $+20^{\circ}\text{C}$ was measured to be 15, while at -20°C and the same
 333 bias voltage it was measured to be 25.

334 The distribution of the signal MPV across the sensor surface is shown in Fig. 15. We
 335 observe that the signal MPV increases by more than a factor of two when the temperature
 336 is reduced from $+20^{\circ}\text{C}$ to -20°C . While the MPV uniformity across the two channels
 337 are within 2% of each other at room temperature, at lower temperatures one of the pixels
 338 shows a difference of about 5% with respect to its neighboring pixel. A more detailed
 339 study is needed to understand whether this difference is due to non-uniform temperature
 340 distribution across the sensor array or due to differences in the signal response between
 341 different pixel sensors at colder temperatures.

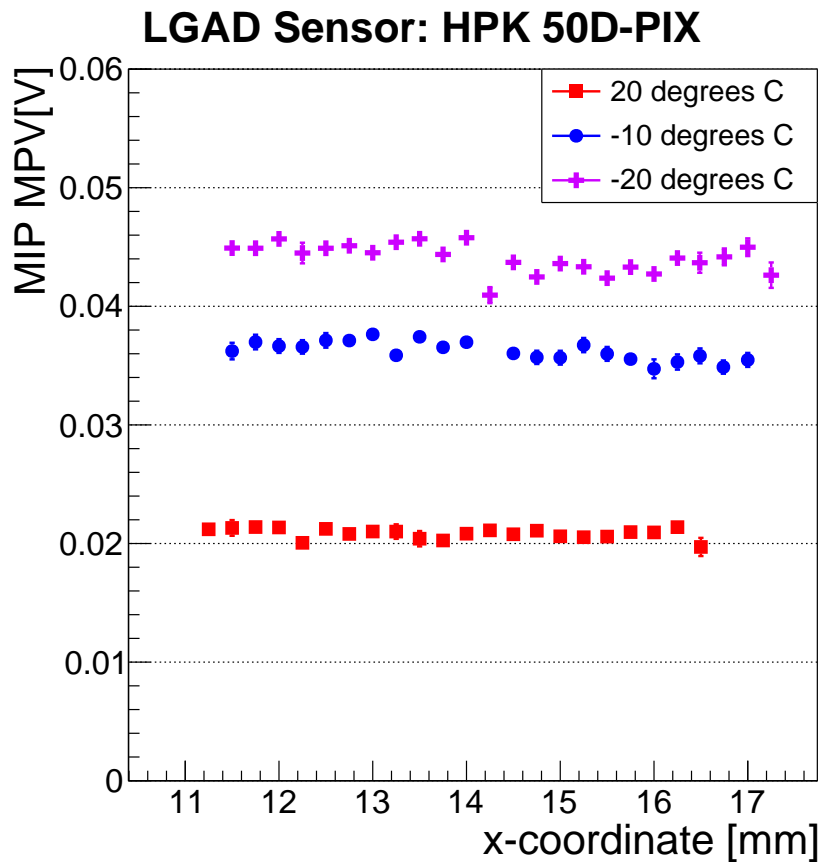


Figure 15: Temperature dependence of the signal amplitude MPV uniformity across the X-axis of the HPK 50D-PIX sensors mounted on the FNAL board. The scan of pixels 1 and 2 along the X-axis is shown, and pixel numbering scheme is defined in Fig. 4. The HPK sensor is biased at -250 V .

342 The distribution of the Δt between the reference timestamp and the timestamp from
 343 the HPK 50D-PIX sensor is shown in Fig. 16. We observe no significant changes in the
 344 behavior of the Δt as the temperature varies.

345 The time resolution measured for the HPK 50D-PIX sensor is shown in Fig. 17. We

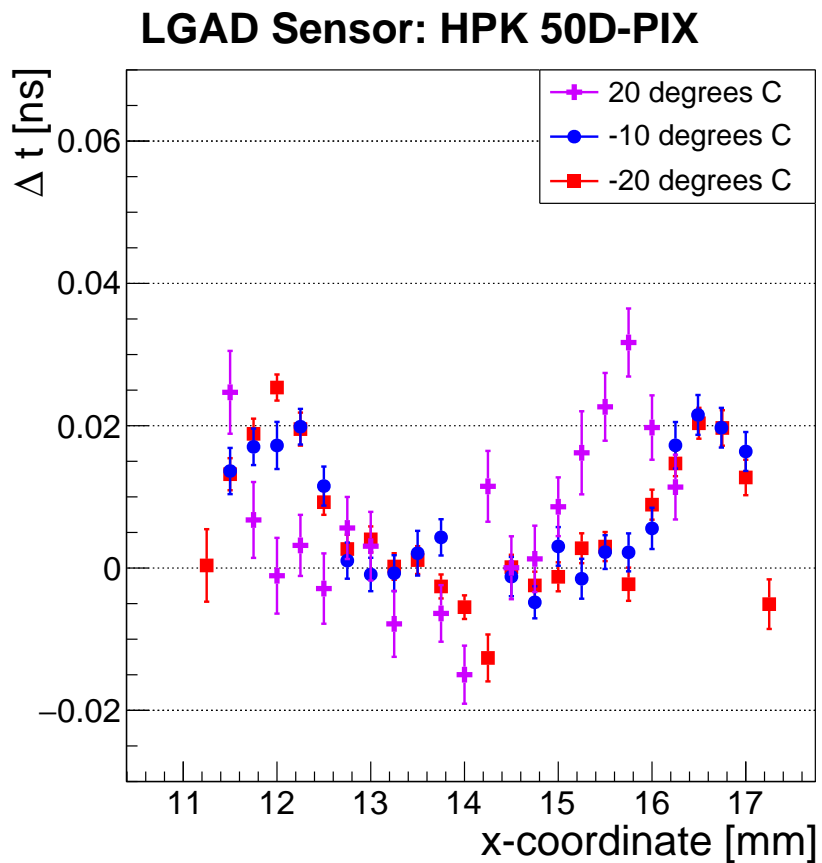


Figure 16: Temperature dependance of the Δt uniformity across the X-axis of the HPK 50D-PIX sensors mounted on the FNAL board. The scan of pixels 1 and 2 along the X-axis is shown, and pixel numberng scheme is defined in Fig. 4. The HPK sensor is biased at -250 V.

346 observe a significant improvement in the time resolution as the temperature is lowered
 347 from +20°C to -20°C degrees. As the temperature is lowered, the signal-to-noise ratio
 348 improves as the gain of the LGAD sensor increases. Generally, the electronic noise may
 349 also decrease as the temperature is lowered, but in our case it was observed to remain
 350 relatively constant at 1.2 mV for both +20 and -20°C. Therefore the improvement comes
 351 mainly from the increase in the signal gain. The time resolution was measured to improve
 352 from around 55-60 ps at the room temperature, down to 35-40 ps at -20°C. It is worth
 353 noting that time resolution around 35 ps with pixels of area 9 mm² is a promising result
 354 for cost-effective implementation in LHC experiments.

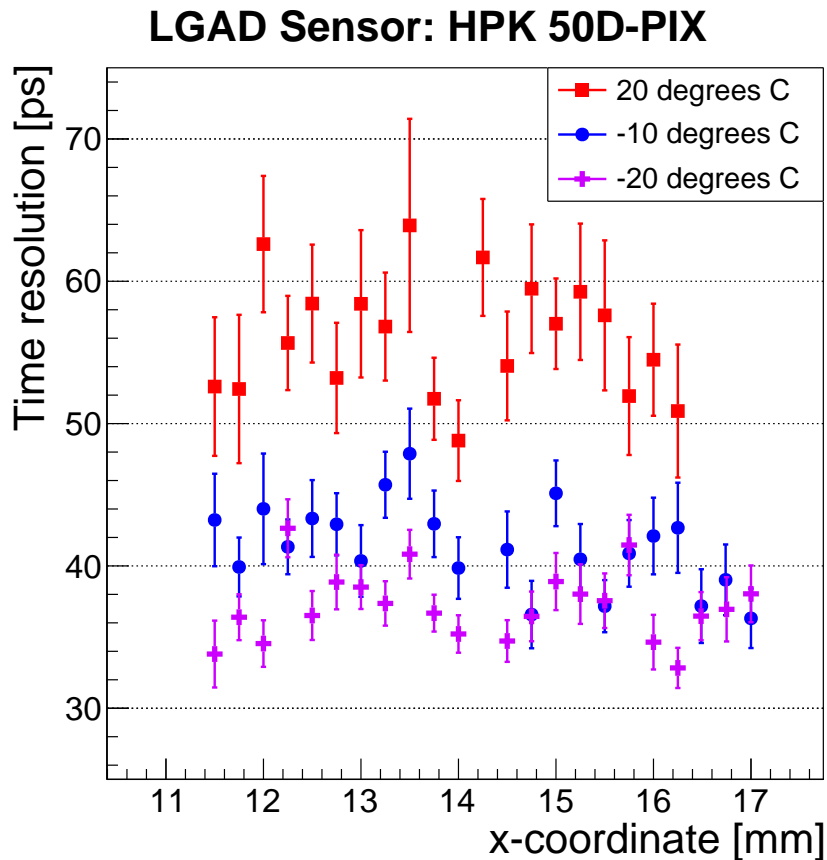


Figure 17: Temperature dependance of the time resolution uniformity across the X-axis of the HPK 50D-PIX sensors mounted on the FNAL board. The scan of pixels 1 and 2 along the X-axis is shown. The pixel numbernig scheme is defined in Fig. 4. The HPK sensor is biased at -250 V.

355 6.6. Radiation tolerance of the LGADs

356 In this section we present the studies of the irradiated HPK and CNM sensors, which
 357 were exposed to neutron irradiation at the Ljubljana TRIGA reactor. The neutron

spectrum and flux are well known and the fluence is quoted in 1 MeV equivalent neutrons per cm^2 ($n_{\text{eq.}}/\text{cm}^2$ or n/cm^2 for short). After $6 \times 10^{14} \text{ n}/\text{cm}^2$ irradiation, the devices were annealed for 80 min at 60°C . Afterward the devices were kept at -20°C degree during storage, transportation, and test beam experiments.

The two-dimensional distribution of the signal amplitudes on the surface of the irradiated sensors are shown in Figs. 18 and 19. From the comparison with the image of the CNM sensor shown in Fig. 4 and the distribution in Fig. 18, it is clear that two distinct regions can be identified on the sensor based on the signal amplitude: the region under the aluminum metallization on the periphery of the sensor, and the region without aluminum metallization in the center. The distribution on the right of Fig. 18 shows that the amplitude under the aluminum (periphery) is about 2.5 times larger than that without aluminum (center). The amplitude scan of the irradiated HPK 50D sensor is shown on the left panel of Fig. 19, and a uniform amplitude across the sensor surface is observed, which can also be seen on the right panel of Fig. 19. In contrast to the CNM sensor, the HPK sensor does not contain any portions that have active area covered with aluminum metallization.

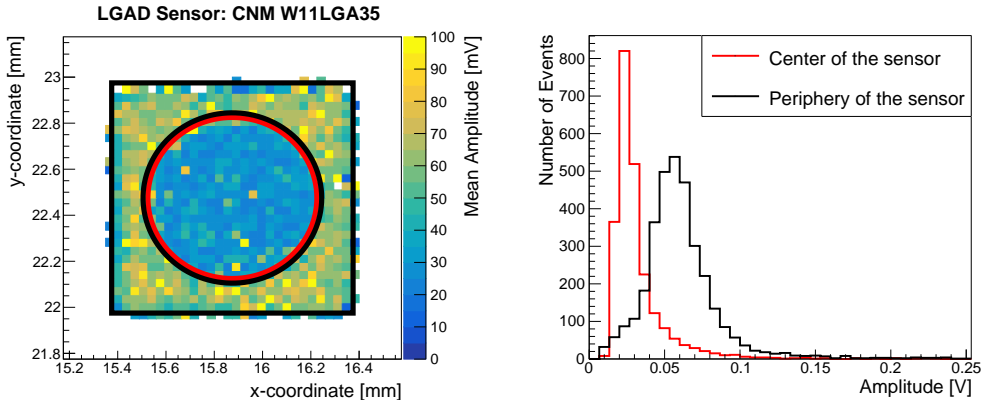


Figure 18: (Left) The map of the amplitude distribution on the irradiated CNM W11LGA35 sensor across X and Y coordinates. Two distinct regions on the sensor surface can be identified according to the amplitude distribution: the center of the sensor (area within the red circle), and the periphery of the sensor (area between the black circle and black square). (Right) Amplitude distribution in the two areas of the irradiated CNM W11LGA35 sensor. The sensor was irradiated to $6 \times 10^{14} \text{ n}/\text{cm}^2$. Measurements were performed at -20°C .

Measurements of the particle detection efficiency are shown in Fig. 20. These measurements were performed with the HPK sensor biased at -600 V , and the CNM sensor biased at -400 V . We observe a flat 100% efficiency across the whole HPK sensor area, and the efficiency of the CNM sensor is also very close to 100%. As with the pixelated array sensors, a clear drop in efficiency is observed near the edges of the active area.

The distribution of MPV of signal amplitudes across the sensor area is shown in Fig. 21, where the MPV is extracted as described in Sec. 6.1. Measurements were performed at two bias voltage values for both sensors: -600 and -635 V for HPK (gain equal to 19 and 29, respectively), and -400 and -420 V for CNM sensors (gain equal to 14 and 15, respectively). A uniform signal amplitude is observed across the HPK sensor,

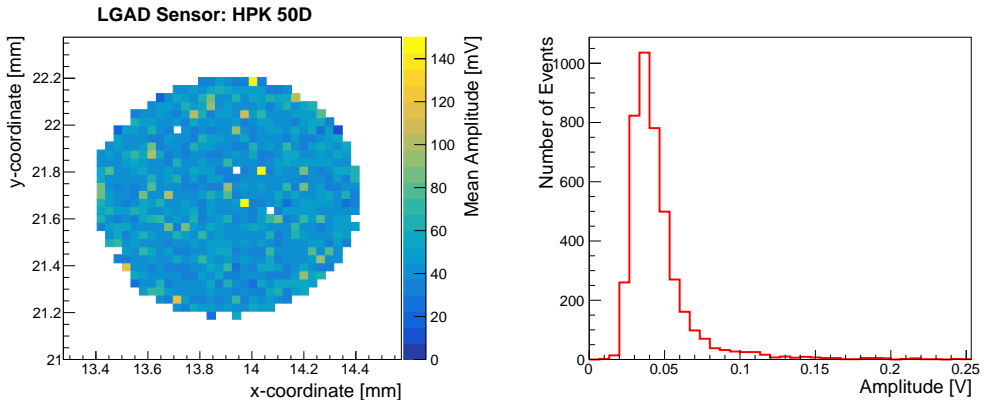


Figure 19: (Left) The map of the amplitude distribution on the irradiated HPK 50D sensor across X and Y coordinates. (Right) Signal amplitude distribution for the irradiated HPK 50D sensor. The sensor was irradiated to 6×10^{14} n/cm². Measurements were performed at -20°C .

384 while for the CNM sensor the amplitude varies across the sensor surface, as observed also
 385 in Fig. 18.

386 The distribution of the Δt between the reference timestamp and the timestamps of the
 387 signals from the irradiated HPK and CNM sensors are shown in Fig. 22. Measurements
 388 at both bias voltage values are presented. We measured a uniform distribution of the
 389 Δt values across the HPK sensor. The CNM sensor exhibits a non-uniformity across the
 390 sensor surface, where the signals from the central, non-metallized area arrive about 10 ps
 391 earlier than those from the peripheral, metallized area.

392 Distributions of the time resolution across the surface of the irradiated sensors are
 393 shown in Fig. 23. The time resolution measured with the HPK sensor improves slightly
 394 with the increase of the bias voltage, and shows a uniform distribution across the sensor
 395 surface. In contrast, the CNM sensor shows a non-uniform distribution of time resolution,
 396 which is a consequence of the variations of the signal amplitude across the sensor. We
 397 do not observe an improvement in the time resolution measured with the CNM sensor
 398 with the increase in the bias voltage.

399 7. Conclusion

400 In a beam test at FNAL with tracking information, we compared the performance
 401 of LGAD produced by CNM Barcelona and HPK Hamamatsu. Single pads of diameter
 402 1 mm and 2×2 arrays of square pixels of 3 mm were used. Sensors with thicknesses of
 403 about 50 and 80 μm were studied. The uniformity of the sensor response in pulse height,
 404 efficiency, and timing resolution were studied. Four different readout boards were used
 405 in these studies. The uniformity of the sensor response in pulse height before irradiation
 406 was found to have a 2% spread. The efficiency and timing resolution before irradiation
 407 were found to be 100% and 30-40 ps, respectively. The “non-response” region between
 408 pixels was measured to be about 70 μm for CNM sensors and 110 μm for HPK sensors. A
 409 small timing shift across the HPK sensor of the order 20–30 ps’ can be explained by the
 410 observed change in pulse shape when comparing metallized and non-metallized sensor

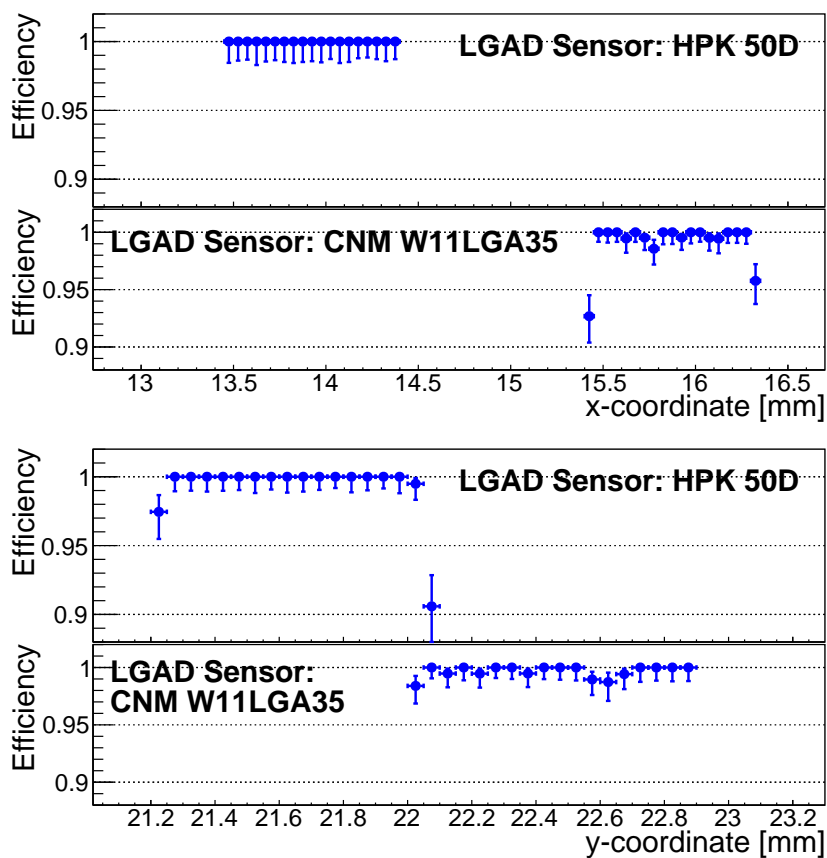


Figure 20: Efficiency measurements across the X-axis (top) and Y-axes (bottom) of the HPK 50D and CNM W11LGA35 irradiated sensors. Both sensors were irradiated to $6 \times 10^{14} \text{ n/cm}^2$. Measurements were performed at -20°C .

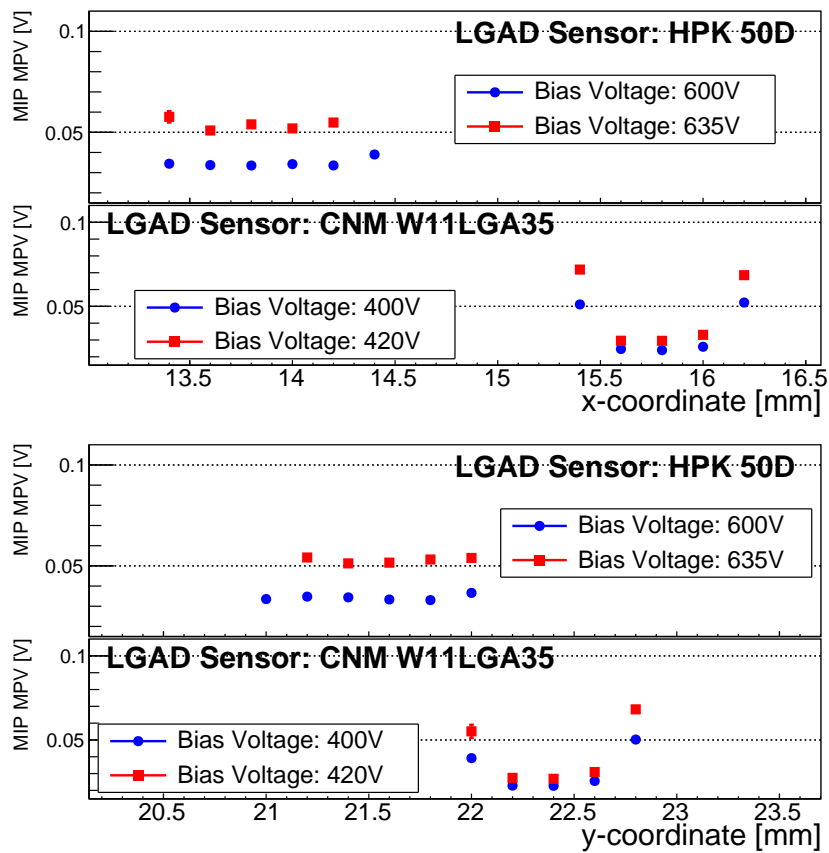


Figure 21: Signal amplitude MPV measurement across the X-axis (top) and Y-axes (bottom) of the HPK 50D and CNM W11LGA35 irradiated sensors. Both sensors were irradiated to $6 \times 10^{14} \text{ n/cm}^2$. Measurements were performed at -20°C .

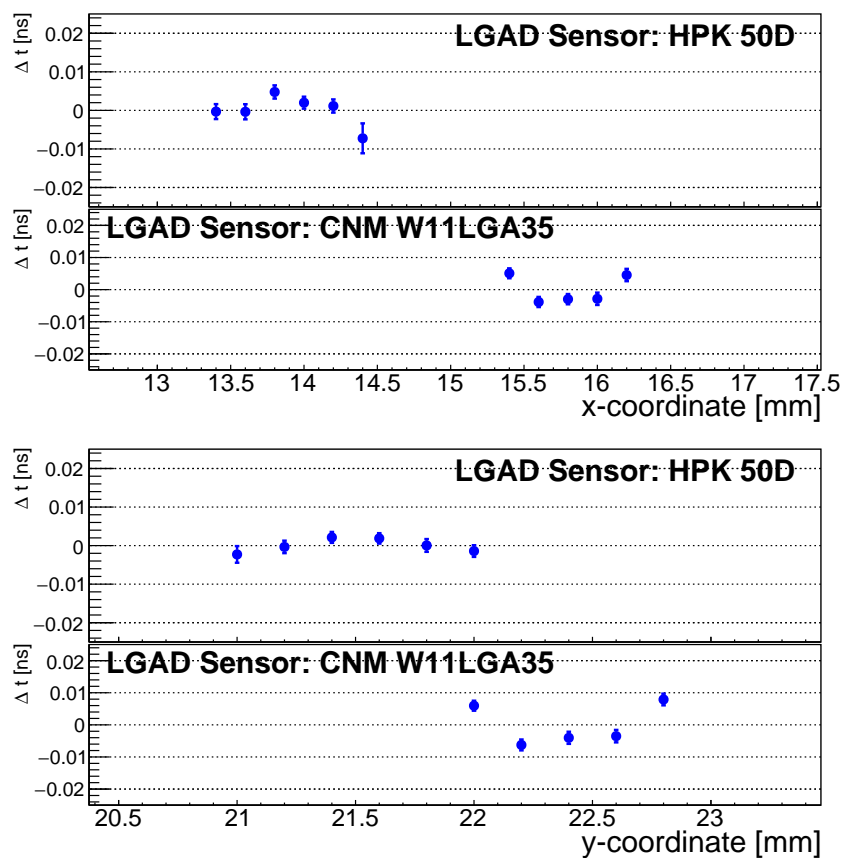


Figure 22: Δt measurements across the X-axis (top) and Y-axes (bottom) of the HPK 50D and CNM W11LGA35 irradiated sensors. Both sensors were irradiated to 6×10^{14} n/cm². Measurements were performed at -20°C .

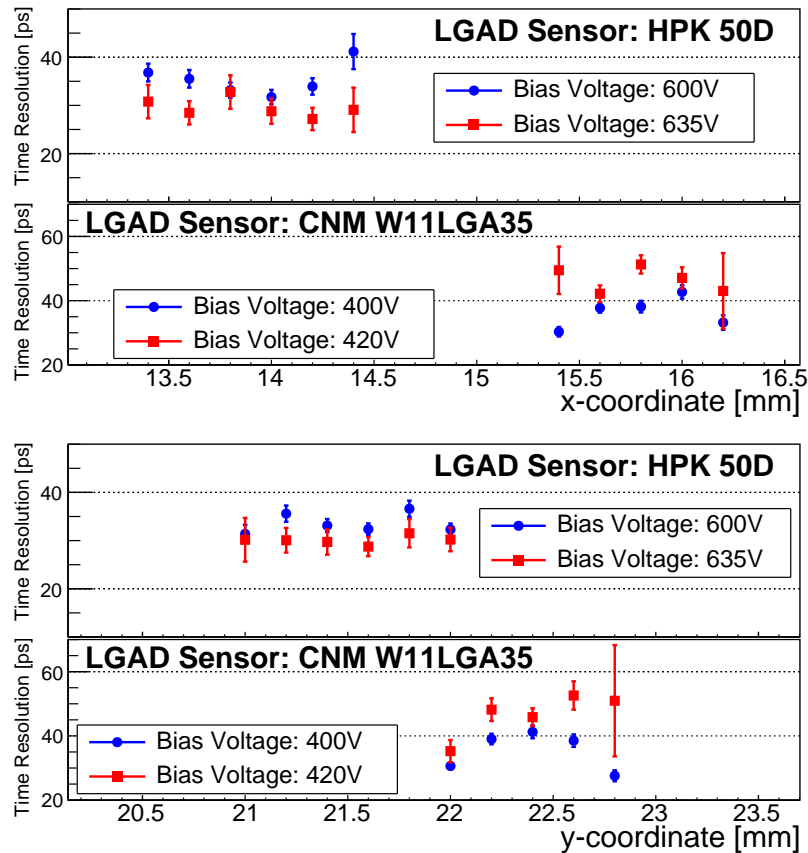


Figure 23: Time resolution measurements across the X-axis (top) and Y-axes (bottom) of the HPK 50D and CNM W11LGA35 irradiated sensors. Both sensors were irradiated to $6 \times 10^{14} \text{ n/cm}^2$. Measurements were performed at -20°C .

411 areas. Uniform signal detection efficiency of 100% is observed on all sensors, both before
412 and after irradiation.

413 For an un-irradiated 50 μm thick LGADs with 3 mm pads we find the following timing
414 results:

- 415 • at a temperature of +20°C, the timing resolution ranges from 40 ps to 50 ps
416 depending on the readout board.
- 417 • cooling the LGAD, while keeping the bias voltage the same at -250 V (**what is**
418 **the gain at -250 V**), improves the timing resolution from 55 ps at +20°C to
419 43 ps at -10°C to 36 ps at -20°C.

420 After a neutron fluence of $6 \times 10^{14} \text{ n/cm}^2$, the single pad CNM sensor exhibits a
421 large gain variation of a factor 2.5 when comparing metallized and non-metallized sensor
422 areas. For an 50 μm thick LGAD with 1 mm pads irradiated $6 \times 10^{14} \text{ n/cm}^2$ we find the
423 following timing results when operated at -20°C:

- 424 • for the HPK LGAD the highest bias voltage reached is -635 V and the correspond-
425 ing timing resolution is 30 ps;
- 426 • for the CNM LGAD the highest bias voltage reached is -420 V and the correspond-
427 ing timing resolution is 30 ps for the metallized area and 40 ps for the non-metallized
428 area.

429 **Acknowledgement**

430 We thank the FTBF personnel and Fermilab accelerator's team for very good beam
431 conditions during our test beam time. We also appreciate the technical support of the
432 Fermilab SiDet department for the rapid production of wire-bonded and packaged LGAD
433 assemblies. We would like to thank Alan Prosser and Ryan Rivera for their critical help
434 in setting up the DAQ and trigger chain. We thank Ned Spencer, Max Wilder, and Forest
435 McKinney-Martinez for their technical assistance, and the CNM and HPK manufacturing
436 team. We acknowledge the help of V. Cindro and I. Mandic with the neutron irradiations.

437 This document was prepared using the resources of the Fermi National Accelerator
438 Laboratory (Fermilab), a U.S. Department of Energy, Office of Science, HEP User Facil-
439 ity. Fermilab is managed by Fermi Research Alliance, LLC (FRA), acting under Contract
440 No. DE-AC02-07CH11359. Part of this work was performed within the framework of
441 the CERN RD50 collaboration.

442 This work was supported by the Fermilab LDRD 2017.027; by the United States
443 Department of Energy grant DE-FG02-04ER41286; by the California Institute of Tech-
444 nology High Energy Physics under Contract DE-SC0011925; by the European Union's
445 Horizon 2020 Research and Innovation funding program, under Grant Agreement no.
446 654168 (AIDA-2020) and Grant Agreement no. 669529 (ERC UFSD669529); by the
447 Italian Ministero degli Affari Esteri and INFN Gruppo V; and by the Spanish Min-
448 istry of Economy, Industry and Competitiveness through the Particle Physics National
449 Program (ref. FPA2014-55295-C3-2-R and FPA2015-69260-C3-3-R) co-financed with
450 FEDER funds.

451 **References**

- 452 [1] A. Apresyan, G. Bolla, A. Bornheim, H. Kim, S. Los, C. Pena, E. Ramberg, A. Ronzhin, M. Spiropulu, and S. Xie, "Test beam studies of silicon timing for use in calorimetry," *Nuclear Instruments and Methods in Physics Research Section A: Accelerators, Spectrometers, Detectors and Associated Equipment*, vol. 825, pp. 62 – 68, 2016.
- 453 [2] A. Apresyan, "Investigation of Fast Timing Capabilities of Silicon Sensors for the CMS High Granularity Calorimeter at HL-LHC," in *Proceedings, 2016 IEEE Nuclear Science Symposium and Medical Imaging Conference (NSS/MIC 2016)*, Oct 2016. <http://2016.nss-mic.org/index.php>.
- 454 [3] N. Akchurin, V. Ciriolo, E. Currs, J. Damgov, M. Fernández, C. Gallrapp, L. Gray, A. Junkes, M. Mannelli, K. M. Kwok, P. Meridiani, M. Moll, S. Nourbakhsh, S. Pigazzini, C. Scharf, P. Silva, G. Steinbrueck, T. T. de Fatis, and I. Vila, "On the timing performance of thin planar silicon sensors," *Nuclear Instruments and Methods in Physics Research Section A: Accelerators, Spectrometers, Detectors and Associated Equipment*, vol. 859, pp. 31 – 36, 2017.
- 455 [4] N. Cartiglia *et al.*, "Beam test results of a 16 ps timing system based on ultra-fast silicon detectors," *Nucl. Instrum. Meth. A*, vol. 850, pp. 83 – 88, 2017.
- 456 [5] G. Pellegrini, P. Fernández-Martínez, M. Baselga, C. Fleta, D. Flores, V. Greco, S. Hidalgo, I. Mandić, G. Kramberger, D. Quirion, and M. Ullan, "Technology developments and first measurements of Low Gain Avalanche Detectors (LGAD) for high energy physics applications," *Nuclear Instruments and Methods in Physics Research Section A: Accelerators, Spectrometers, Detectors and Associated Equipment*, vol. 765, pp. 12 – 16, 2014. HSTD-9 2013 - Proceedings of the 9th International.
- 457 [6] Z. Galloway *et al.*, "Properties of HPK UFSD after neutron irradiation up to 6e15 n/cm²," 2017. arXiv/1707.04961 [physics.ins-det].
- 458 [7] S. Kwan, C. Lei, D. Menasce, L. Moroni, J. Ngadiuba, A. Prosser, R. Rivera, S. Terzo, M. Turqueti, L. Uplegger, L. Vigani, and M. E. Dinardo, "The pixel tracking telescope at the fermilab test beam facility," *Nuclear Instruments and Methods in Physics Research Section A: Accelerators, Spectrometers, Detectors and Associated Equipment*, vol. 811, pp. 162 – 169, 2016.
- 459 [8] D. Anderson, A. Apresyan, A. Bornheim, J. Duarte, C. Pena, A. Ronzhin, M. Spiropulu, J. Trevor, and S. Xie, "On Timing Properties of LYSO-Based Calorimeters," *Nucl. Instrum. Meth. A*, vol. 794, pp. 7–14, 2015.
- 460 [9] A. Ronzhin, S. Los, E. Ramberg, M. Spiropulu, A. Apresyan, S. Xie, H. Kim, and A. Zatserklyaniy, "Development of a new fast shower maximum detector based on microchannel plates photomultipliers (MCP-PMT) as an active element," *Nucl. Instrum. Meth. A*, vol. 759, pp. 65 – 73, 2014.
- 461 [10] A. Ronzhin, S. Los, E. Ramberg, A. Apresyan, S. Xie, M. Spiropulu, and H. Kim, "Study of the timing performance of micro-channel plate photomultiplier for use as an active layer in a shower maximum detector," *Nucl. Instrum. Meth. A*, vol. 795, pp. 288 – 292, 2015.
- 462 [11] A. Ronzhin, S. Los, E. Ramberg, A. Apresyan, S. Xie, M. Spiropulu, and H. Kim, "Direct tests of micro channel plates as the active element of a new shower maximum detector," *Nucl. Instrum. Meth. A*, vol. 795, pp. 52 – 57, 2015.
- 463 [12] <http://www.caen.it/csite/CaenProd.jsp?parent=11&idmod=661>.
- 464 [13] H. Kim, C.-T. Chen, N. Eclov, A. Ronzhin, P. Murat, E. Ramberg, S. Los, W. Moses, W.-S. Choong, and C.-M. Kao, "A new time calibration method for switched-capacitor-array-based waveform samplers," *Nucl. Instrum. Meth. A*, vol. 767, pp. 67 – 74, 2014.
- 465 [14] M. Carulli *et al.*, "First 50 m thick LGAD fabrication at CNM." <https://agenda.infn.it/getFile.py/access?contribId=20&sessionId=8&resId=0&materialId=slides&confId=11109>, 2016. 28th RD50 Workshop, Torino.
- 466 [15] <http://www.caen.it/csite/CaenProd.jsp?parent=11&idmod=661>.
- 467 [16] H. Kim, C.-T. Chen, N. Eclov, A. Ronzhin, P. Murat, E. Ramberg, S. Los, W. Moses, W.-S. Choong, and C.-M. Kao, "A new time calibration method for switched-capacitor-array-based waveform samplers," *Nucl. Instrum. Meth. A*, vol. 767, pp. 67 – 74, 2014.
- 468 [17] M. Carulli *et al.*, "First 50 m thick LGAD fabrication at CNM." <https://agenda.infn.it/getFile.py/access?contribId=20&sessionId=8&resId=0&materialId=slides&confId=11109>, 2016. 28th RD50 Workshop, Torino.